Theoretical Investigation of Two-State-Reactivity Pathways of H−H Activation by FeO^+: Addition−Elimination, "Rebound", and Oxene-Insertion Mechanisms

Michael Filatov and Sason Shaik*

Department of Organic Chemistry and the Lise Meitner-Minerva Centre for Computational Quantum Chemistry, The Hebrew University, 91904 Jerusalem, Israel

Received: January 28, 1998

Density functional calculations using the B3LYP, BP86, and FT97 functionals with an extended basis set are employed to investigate the mechanisms of H_2 oxidation by FeO^+. Three mechanisms are considered, addition−elimination, "rebound", and oxene-insertion. The oxene-insertion is characterized by high barriers and only second-order saddle points. The addition−elimination and "rebound" mechanisms are competitive and both exhibit two-state-reactivity (TSR) with a crossing between sextet and quartet states. TSR provides a low-energy path for bond activation and is predicted to be the dominant pathway at room temperature. Both TSR mechanisms are concerted: the addition−elimination mechanism involves 2+2 addition in the bond activation step, while the rebound mechanism is effectively concerted involving the H-abstraction followed by a barrierless "rebound" of the H-radical. At elevated temperature (above a threshold of $^3/_2RT = 0.5$ eV), the stepwise "rebound" mechanism starts to dominate and produces $FeOH^+ + H^\bullet$ via a single-state-reactivity (SSR) on the sextet surface. Kinetic isotope effect calculations have been performed, and their comparison with the experimental data[10] seems to be characteristic of TSR. Thus, the measured isotope effects probe the extent of H···H (D···D) cleavage in a mechanism whereby bond activation and spin-inversion occur in a concerted manner. Some predictions have been made regarding the factors that affect the mechanistic competition.

Introduction

The gas-phase oxidation of H_2 by bare FeO^+, eq 1, has drawn considerable experimental and theoretical effort in recent years.[1−4]

$$FeO^+(^6\Sigma^+) + H_2 \rightarrow Fe^+(^6D) + H_2O \qquad (1)$$

A great part of the attraction has been certainly the stipulation that this reaction may serve as a model that will shed light on the mechanism of hydrocarbon oxidation by transition metal oxenids in liquid phase and in enzymatic systems.[5] As such, the mechanism of reaction 1 is a truly fundamental problem that is still only partly resolved.[6] Let us then note briefly some of these mechanistic questions.

The initial mechanistic puzzle[2] has been associated with the root cause of the poor efficiency ($\Phi \approx 10^{-2}-10^{-3}$) of this reaction, which is exothermic ($\Delta H^\circ_R = -37$ kcal/mol), orbitally unrestricted, and spin-allowed. Theoretical considerations and calculations[3,7] of the addition−elimination mechanism, Scheme 1, have shown that the apparent spin-allowedness originates in a *double crossing of the high-spin and low-spin surfaces* along the reaction coordinate. It has been postulated[3,7] that it is the low probability of crossing the spin-inversion junctions that impairs the rosy prospects of the reaction. This has been later vindicated by detailed spin−orbit coupling calculation[8] which revealed that the probability of spin-crossover in the bond-activation step (point 1, Scheme 1) is quite low ($10^{-2}-10^{-3}$) and can give rise to the poor oxidative efficiency.

This electronic mechanism, which has been called a *two-state-reactivity (TSR) mechanism,*[8,9] *provides a low-energy pathway for the bond activation along with the problem of spin-crossover.* Recent experimental studies by multiple mass spectrometric techniques[10] of the oxidations of H_2 and CH_4 have shown the likelihood of the TSR mechanistic scenario, but have also raised a host of new questions. Thus, while the temperature profile[10] of the efficiency may be suggestive[8,10] of the nonadiabatic nature of the spin-inversion problem, still it is not conclusive that the reaction's bottleneck is not the barrier on the low-spin surface (Scheme 1).[10] Indeed, the calculation done so far[7] suggests a significant barrier (6 kcal/mol) on the surface. An associated problem is the origins of the very small isotope effect, $k_{H_2}/k_{D_2} \approx 1-1.5$, which is measured[10] for this reaction. Is the low value consistent with a TSR mechanism? Finally, the guided beam and ion-cyclotron techniques[2,10] have shown[10] that above a threshold of kinetic energy, ca. 0.5 eV, another process is observed: the formation of $FeOH^+$ in eq 2. Since

SCHEME 1: Two-State-Reactivity (TSR) in the Addition−Elimination Mechanism

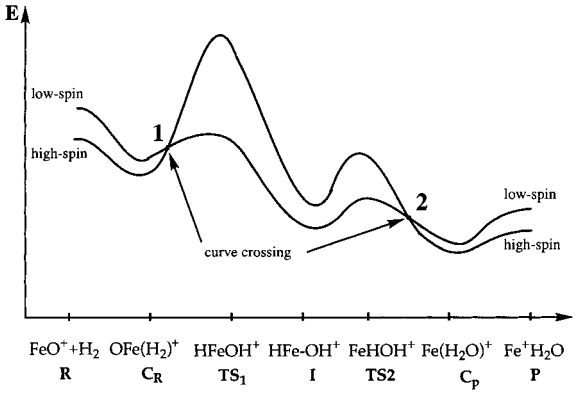

* E-mail address: sason@yfaat.ch.huji.ac.il. Fax: +972-2-6585345.

S1089-5639(98)00929-3 CCC: $15.00
Published on Web 04/30/1998

SCHEME 2

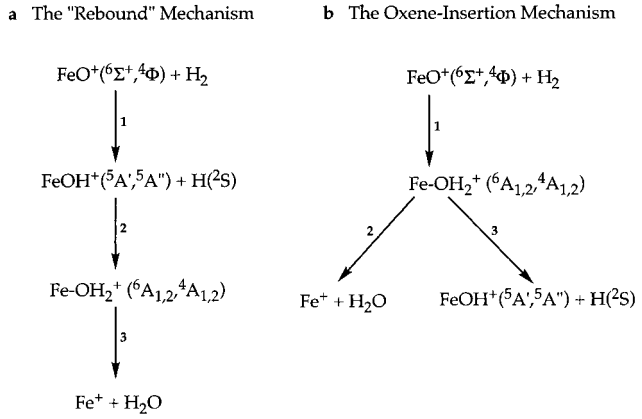

this kind of product prevails in the oxidation of CH_4,[11]

$$FeO^+(^6\Sigma^+) + H_2 \rightarrow FeOH^+(^5A') + H(^2S) \qquad (2)$$

a mechanistic question regarding the pathway that forms $FeOH^+$ needs to be addressed. Thus, by analogy with the reactions of MnO^+ with H_2[12] here too $FeOH^+$ may originate[10] from the dissociation processes in eqs 3a and 3b.

$$(HFe-OH)^+ \rightarrow FeOH^+ + H^\bullet \qquad (3a)$$

$$(Fe-OH_2)^+ \rightarrow FeOH^+ + H^\bullet \qquad (3b)$$

If this was indeed the case, the addition−elimination mechanism would account completely for the reactivity features of FeO^+/H_2. However, an alternative mechanism for $FeOH^+$ production is the "rebound" mechanism[13] shown in Scheme 2a, where the initial step involves a hydrogen abstraction followed by a "rebound" of the $H^\bullet$ on the OH moiety to form the $Fe-OH_2^+$ complex. In this mechanism the $FeOH^+$ is an intermediate product en route to the final oxidation products.

Yet another potential mechanism is the oxene-insertion, Scheme 2b, which produces $Fe-OH_2^+$ in a single concerted steps analogous to carbene insertion. Here too the $FeOH^+$ may be a byproduct of the $Fe-OH_2^+$ decomposition.

The "rebound" mechanism is the prevailing paradigm in the enzymatic oxidations by P-450 cytochrome,[13] and recently[14] the oxene-insertion has been suggested as a possible mechanism for these reactions. Thus, it is important to investigate these mechanisms (see Scheme 2) along with the addition−elimination mechanism (Scheme 1) and assess their relative importance.

The problem at hand is complex and multifaceted. There exist three candidate mechanisms, see Schemes 1 and 2, with their own specific problems. Are all of them equally feasible? Are the "rebound" and oxene-insertion truly spin-conserving, as drawn in Scheme 2, or are they concealed spin-forbidden reactions attended by double crossings like in the addition−elimination mechanism in Scheme 1? Finally, how do these mechanisms or any combination thereof account for the reactivity features probed by experiments?[10]

To tackle these questions, we perform quantum chemical calculations of potential energy surfaces and kinetic isotope effect factors for the three mechanisms. Our method of choice is the density functional theory (DFT), using three different functionals, pure as well as a hybrid, in a comparative study that allows reasonable judgement. This along with a sufficiently large basis set may provide a reasonably accurate description of the mechanistic issues.

Method of Calculation

Density functional calculations have been performed with CADPAC6[15] and CADPAC5[16] packages and employ a high-quality grid for numerical integration which includes 110 radial integration shells and 302 integration points per radial shell (Lebedev grid of 29th order). Three different density functionals have been employed: pure density functional BP86[16] and hybrid HF/DFT functional B3LYP[17] as implemented in the CADPAC6[15] suite of programs and recently developed FT97 density functional[18] implemented in the CADPAC5 package.[16] The comparison of qualitative predictions from different functionals is required in order to judge the stability and consistency of the predictions. Should the predictions be inconsistent, this would require additional calculations using more sophisticated quantum-chemical methods. As shall be seen later, the descriptions of the three mechanisms is consistent and stable with the three functionals, and therefore additional tests are not warranted.

All density functional calculations employ the Wachters[19] (8s6p4d) basis on the metal and the Dunning−Huzinaga triple-zeta double polarization[20] (TZ2P) basis on the light atoms. These fairly large basis sets are prerequisite for getting results that are sufficiently stable against further basis set extension. The spin-unrestricted formalism has been used for all open-shell species.

The $\langle S^2 \rangle$ values are reported for all calculated stationary points. This is done to examine the degree of spin contamination in the wave functions of the noninteracting particles yielded by the Kohn−Sham method. Thus, while these $\langle S^2 \rangle$ values do not refer to the actual many-body wave function, they do characterize the extent to which the reference wave function of noninteracting particles *is adequate to approximate the correct spin-symmetry* of the real wave function.

Most calculations have been performed within the C_s symmetry constraint with the exception of a few cases where unconstrained optimization yielded lower total energies (see below). All critical points have been characterized by vibrational analysis.

Kinetic isotope effects (KIEs) have been calculated using transition-state theory,[21] which leads to the following expression.

$$\frac{k_{H_2}}{k_{D_2}} = \left(\frac{m_D^R}{m_H^R}\frac{m_H^\#}{m_D^\#}\right)^{3/2} \frac{I_{D_2}}{I_{H_2}} \left(\frac{I_{x_H}^\# I_{y_H}^\# I_{z_H}^\#}{I_{x_D}^\# I_{y_D}^\# I_{z_D}^\#}\right)^{1/2} \frac{q_{v_D}^R}{q_{v_H}^R}\frac{q_{v_H}^\#}{q_{v_D}^\#} \times \exp\left(-\frac{E_H^\# - E_D^\#}{RT}\right) \qquad (4)$$

where subscripts H and D denote quantities belonging to the hydrogen- and deuterium-substituted systems, respectively; superscripts R and # denote quantities belonging to the reactants and activation complex; q_v stands for the vibrational partition function; $I_x(y,z)$ are principal moments of inertia; m is molecular mass; and $E^\#$ is activation energy calculated with respect to the reactants in their respective ground states and includes the zero-point vibrational energies (ZPE) and thermal corrections to finite temperature.

Results

The results are described by appeal to the mechanisms specified in Schemes 1 and 2. The data are summarized in Tables 1 and 2 and Figures 1 and 2. The trends obtained by the three functionals are consistent and lead to a uniform qualitative picture of reactivity. The B3LYP hybrid functional

TABLE 1: Summary of the Results for the Addition−Elimination Mechanism of the $FeO^+ + H_2$ Reaction

entry	molecule	FT97	BP86	B3LYP
1	$FeO^+(^6\Sigma^+)/H_2$			
	total energy, au	−1339.816 578	−1339.954 696	−1339.621 975
	Fe−O, Å	1.659	1.639	1.643
	H−H, Å	0.745	0.747	0.740
	$\langle S^2\rangle$	8.762	8.758	8.769
2	$FeO^+(^4\Phi)/H_2$			
	total energy, au	−1339.791 885	−1339.934 456	−1339.609 252
	Fe−O, Å	1.628	1.613	1.703
	H−H, Å	0.745	0.747	0.740
	$\langle S^2\rangle$	4.006	3.997	4.496
3	**1**-^{6}A′			
	total energy, au	−1339.836 271	−1339.980 693	−1339.646 389
	Fe−O, Å	1.667	1.645	1.651
	Fe−H, Å	1.973	1.953	1.983
	H−H, Å	0.775	0.781	0.769
	$\langle S^2\rangle$	8.764	8.759	8.771
4	**1**-^{4}A″			
	total energy, au	−1339.835 897	−1339.980 672	−1339.632 839
	Fe−O, Å	1.588	1.576	1.569
	Fe−H, Å	1.669	1.675	1.765
	H−H, Å	0.850	0.846	0.799
	α, deg[a]	97.2	96.8	98.4
	$\langle S^2\rangle$	3.774	3.771	3.842
5	**TS1**-^{6}A′			
	total energy, au	−1339.797 400	−1339.943 778	−1339.608 515
	Fe−O, Å	1.760	1.737	1.733
	Fe−H′,O A	1.756	1.782	1.797
	O−H, Å	1.310	1.325	1.317
	H−H′, Å	1.089	1.040	1.017
	FeOH, deg	68.3	69.3	70.7
	H′FeO, deg	79.7	78.3	76.7
	-iω, cm^{-1}	1647.75	1559.43	1643.86
	$\langle S^2\rangle$	8.764	8.758	8.771
6	**TS1**-^{4}A″			
	total energy, au	−1339.817 959	−1339.954 745	−1339.620 991
	Fe−O, Å	1.643	1.627	1.624
	Fe−H′, Å	1.628	1.704	1.689
	O−H, Å	1.397	1.409	1.439
	H−H′, Å	0.997	0.967	0.927
	FeOH, deg	66.7	69.2	68.3
	H′FeO, deg	84.7	82.1	82.2
	-iω, cm^{-1}	1143.09	1058.28	999.57
	$\langle S^2\rangle$	3.781	3.787	3.869
7	**2**-^{6}A′			
	total energy, au	−1339.858 093	−1340.007 586	−1339.682 379
	Fe−O, Å	1.775	1.757	1.743
	Fe−H′, Å	1.591	1.587	1.587
	O−H, Å	0.979	0.980	0.969
	FeOH, deg	135.8	135.1	140.3
	H′FeO, deg	146.8	142.5	139.7
	$\langle S^2\rangle$	8.762	8.757	8.762
8	**2**-^{4}A″			
	total energy, au	−1339.871 133	−1340.019 623	−1339.687 204
	Fe−O, Å	1.700	1.690	1.696
	Fe−H′, Å	1.512	1.507	1.523
	O−H, Å	0.979	0.981	0.970
	FeOH, deg	128.7	128.6	129.3
	H′FeO, deg	91.6	89.7	91.2
	$\langle S^2\rangle$	3.811	3.804	3.895
9	**TS2**-^{6}A′			
	total energy, au	−1339.809 890	−1339.965 605	−1339.642 426
	Fe−O, Å	1.840	1.817	1.804
	O−H, Å	0.983	0.984	0.971
	Fe−H′, Å	1.703	1.672	1.715
	O−H′, Å	1.461	1.518	1.608
	FeOH, deg	172.0	171.6	173.8
	H′FeO, deg	48.5	51.4	54.3
	-iω, cm^{-1}	1288.54	1177.97	1029.48
	$\langle S^2\rangle$	8.761	8.755	8.758
10	**TS2**-^{4}A″			
	total energy, au	−1339.849 855	−1340.003 307	−1339.675 795
	Fe−O, Å	1.786	1.766	1.762
	O−H, Å	0.979	0.979	0.968
	Fe−H′, Å	1.608	1.585	1.588

TABLE 1 (Continued)

entry	molecule	FT97	BP86	B3LYP
	O−H′, Å	1.436	1.463	1 556
	FeOH, deg	127.8	131.2	134 6
	H′FeO, deg	49.7	51.4	55 0
	H′FeOH, deg	69.9	60.9	52.5
	-iω, cm^{-1}	1032.94	981.70	862.74
	$\langle S^2 \rangle$	3.843	3.832	3.976
11	**3**-^{6}A′			
	total energy, au	−1339.877 718	−1340.040 668	−1339.739 009
	Fe−O, Å	2.119	2.083	2.100
	O−H, Å	0.976	0.978	0.969
	FeOH, deg	126.3	126.1	126.1
	$\langle S^2 \rangle$	8.752	8.751	8.752
12	**3**-^{4}A″			
	total energy, au	−1339.895 608	−1340.053 714	−1339.747 586
	Fe−O, Å	2.012	2.006	2.041
	O−H, Å	0.971	0.973	0.965
	FeOH, deg	125.9	125.8	126.0
	$\langle S^2 \rangle$	3.826	3.788	3.818
13	$Fe^+(^6D)/H_2O$			
	total energy, au	−1339.828 877	−1339.960 773	−1339.683 388
	O−H, Å	0.968	0.971	0.961
	HOH, deg	103.8	104.4	105.0
	$\langle S^2 \rangle$	8.752	8.751	8.752
14	$Fe^+(^4F)/H_2O$			
	total energy, au	−1339.839 207	−1339.967 659	−1339.687 136
	O−H, Å	0.968	0.971	0.961
	HOH, deg	103.8	104.4	105.0
	$\langle S^2 \rangle$	3.893	3.753	3.754

[a] Angle between the Fe−O bond and the direction to the H−H bond midpoint.

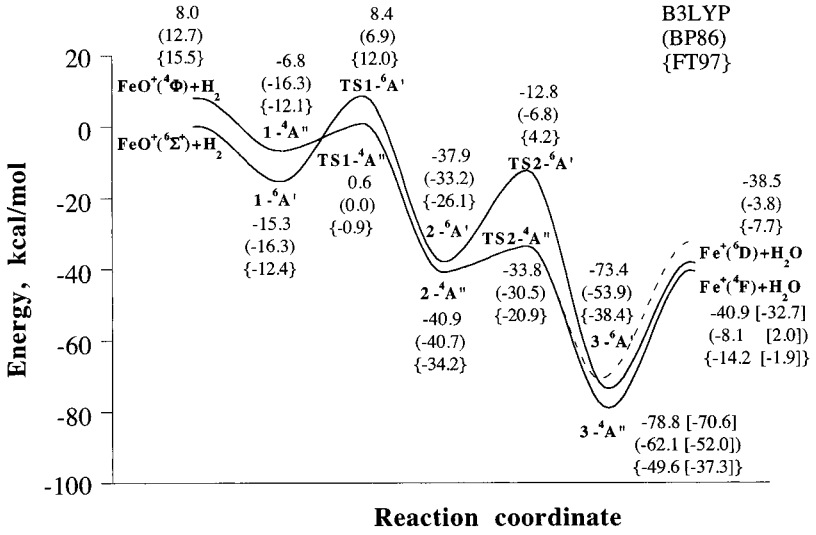

Figure 1. Energy profile for the addition−elimination mechanism. Energies (in kcal/mol units) are given relative to the sextet reactants. The high- and low-spin potential curves are plotted based on B3LYP data, which are given without parentheses. The BP86 data are given parenthetically; the FT97 are given in curly brackets. The dashed line and the numbers in the square brackets correspond to shifted low-spin potential curve (see text).

appears to enjoy a quantitative edge over the pure functionals and reproduces better the known thermochemica1 quantities.

1. Reactants. In agreement with previous results for FeO^+,[7] the present calculations predict a sextet $^6\Sigma^+$ ground state whose configuration is $1\sigma^2 1\pi^4 1\delta^2 2\pi^2 2\sigma^1$. The dissociation energies D_e are 108.0 (FT97), 108.4 (BP86), and 80.5 (B3LYP) kcal/mol. The experimental estimate for the FeO^+ bond energy is 81.4 ± 1.4 kcal/mol.[22] The B3LYP result is very good and responsible for the overall better thermochemical quantities produced by this method throughout the paper.

The excited-state configuration of FeO^+ corresponds to $1\sigma^2 1\pi^4 1\delta^3 2\pi^1 2\sigma^1$ and within C_{2v} and C_s point groups belongs to B_2 and A″ irreducible representations, respectively.[8] This configuration can be interpreted to arise from the $^4\Phi/^4\Pi$ state combination in a $C_{\infty v}$ symmetry group. The excitation energies from density functionals are 0.67 (FT97), 0.55 (BP86), and 0.35 (B3LYP) eV. Previous CASPT2 calculations yield 0.5−0.8 eV for the excitation energy.[7,9] The B3LYP functional underestimates slightly the excitation energy and yields for the quartet state a longer FeO bond in comparison with other density functionals.

2. Addition−Elimination Mechanism. The reaction profile is shown in Figure 1 along with relative energies from the three density functionals. The general features are similar to the partial profile of Fiedler et al.[7] The present profile is complete and includes the transition states of the elimination step which were not investigated previously.[7] Scheme 3 depicts structures and provides structural details.

A. Reactants Complex. In agreement with previous results,[7] in the sextet state the reactants form a planar C_{2v}

TABLE 2: Summary of the Results for the Oxene-Insertion and "Rebound" Mechanisms for the $FeO^+ + H_2$ Reaction

entry	molecule	FT97	BP86	B3LYP
1	**4**-^{4}A″			
	total energy, au	−1339.793 962	−1339.940 169	
	FeO, Å	1.642	1.627	
	HH, Å	0.768	0.774	
	FeH, Å	2.096	2.060	
	α, deg[a]	120.7	120.8	
	$\langle S^2\rangle$	4.077	4.063	
2	"**TS3**"-^{6}A′			
	total energy, au	−1339.754 502	−1339.908 327	−1339.585 208
	FeO, Å	1.794	1.772	1.786
	FeH, Å	1.358	1.436	1.415
	HH, Å	0.932	0.894	0.880
	α, deg[a]	143.2	138.7	135.0
	-iω_1	1640.20	1056.66	1448.83
	-iω_2	1196.82	1178.56	1198.64
	$\langle S^2\rangle$	8.756	8.756	8.760
3	"**TS3**"-^{4}A″			
	total energy, au	−1339.779 966	−1339.931 692	−1339.599 750
	FeO, Å	1.745	1.715	1.741
	FeH, Å	1.381	1.419	1.405
	HH, Å	0.900	0.881	0.868
	α, deg[a]	126.2	127.3	128.6
	-iω_1	1256.95	1094.26	1281.82
	-iω_2	769.64	858.28	956.73
	$\langle S^2\rangle$	4.056	4.099	4.284
4	**5**-^{4}A″			
	total energy, au	−1339.796 714		
	FeO, Å	1.657		
	OH, Å	1.539		
	HH′, Å	0.801		
	FeOH, deg	126.3		
	OHH′, deg	170.9		
	$\langle S^2\rangle$	4.137		
5	**TS4**-^{6}A′			
	total energy, au	−1339.786 772	−1339.937 405	−1339.606 997
	FeO, Å	1.732	1.709	1.733
	OH, Å	1.150	1.210	1.340
	HH′, Å	1.036	0.957	0.851
	FeOH, deg	125.5	123.1	112.9
	OHH′, deg	177.9	177.9	168.6
	-iω	1957.23	1867.28	1922.93
	$\langle S^2\rangle$	8.761	8.760	8.770
6	**TS4**-^{4}A″			
	total energy, au	−1339.794 913		
	FeO, Å	1.701		
	OH, Å	1.166		
	HH′, Å	0.973		
	FeOH, deg	130.7		
	OHH′, deg	174.6		
	-iω	855.26		
	$\langle S^2\rangle$	4.406		
7	**6**-^{6}A′			
	total energy, au		−1339.948 470	−1339.632 327
	FeO, Å		1.721	1.723
	OH, Å		0.994	0 974
	HH′, Å		1.642	1.815
	FeOH, deg		132.3	136.2
	OHH′, deg		189.3	187.4
	$\langle S^2\rangle$		8.756	8.759
8	**6**-^{4}A″			
	total energy, au		−1339.950 630	−1339.632 778
	FeO, Å		1.712	1.719
	OH, Å		1.012	0.977
	HH′, Å		1.415	1.722
	FeOH, deg		132.9	137.2
	OHH′, deg		182.3	183.4
	$\langle S^2\rangle$		4.672	4.735
9	$FeOH^+$(^{5}A′)+H			
	total energy, au	−1339.794 529	−1339.945 200	−1339.630 795
	FeO, Å	1.734	1.723	1.725
	OH, Å	0.975	0.978	0.966
	FeOH, deg	133.3	131.4	136.0
	$\langle S^2\rangle$[b]	6.007	6.006	6.008

TABLE 2: (Continued)

entry	molecule	FT97	BP86	B3LYP
10	$FeOH^+(^5A'')+H$			
	total energy, au	−1339.794 442	−1339.945 072	−1339.630 716
	FeO, Å	1.733	1.722	1.724
	OH, Å	0.975	0.977	0.966
	FeOH, deg	134.4	132.4	136.9
	$\langle S^2\rangle^b$	6.007	6.006	6.008
11	$FeOH^+(a\text{-}^5A')+H$			
	total energy, au	−1339.777 425	−1339.927 824	−1339.612 614
	FeO, Å	1.777	1.758	1.759
	OH, Å	0.980	0.981	0.969
	FeOH, deg	119.5	120.0	123.2
	$\langle S^2\rangle^b$	6.012	6.011	−6.016

[a] Angle between the Fe−O bond and the direction to the H−H bond midpoint. [b] The $\langle S^2\rangle$ value for the $FeOH^+$ molecule.

SCHEME 3: B3LYP Geometries (Table 1) for Species in the Addition−Elimination Mechanism

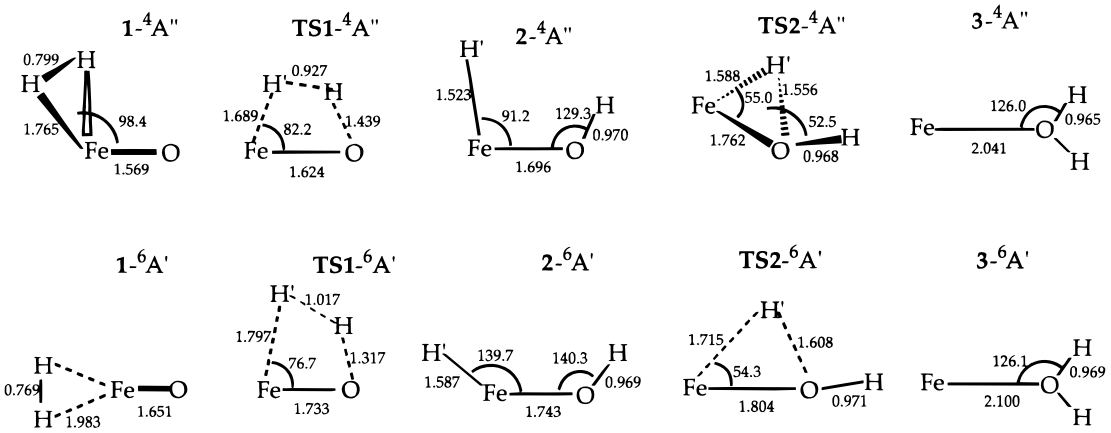

symmetric side-on complex, **1**-^{6}A′ in Scheme 3, with the hydrogen molecule adjacent to the iron. All density functionals predict substantial interaction energy varying from 6.8 kcal/mol (B3LYP) to 16.3 kcal/mol (BP86). The bonding is due to the charge transfer from the σ-orbital of dihydrogen to the empty 3σ-orbital of the FeO^+ fragment. The amount of transferred charge is 0.222*e* (FT97), 0.294*e* (BP86), and 0.214*e* (B3LYP).

In the quartet state, H_2 forms a nonplanar side-on C_s symmetric complex, **1**-^{4}A″ in Scheme 3. This complex is stabilized via interaction of dihydrogen orbitals with δ-type orbitals of Fe^+: donation from the σ-orbital of H_2 to the singly occupied x^2-y^2-orbital of Fe^+ and weak back-donation from the doubly occupied xy-orbital of Fe^+ to the empty σ^*-orbital of H_2. The total charge transfer amounts to 0.284*e* (FT97), 0.278*e* (BP86), and 0.248*e* (B3LYP). Due to larger charge transfer, the resulting interaction energy is higher than in the sextet complex and consists of 27.6 (FT97), 29.0 (BP86), and 14.8 (B3LYP) kcal/mol. As a result, the quartet and sextet surfaces approach one another. The pure density functionals, FT97 and BP86, predict almost equal total energies for the quartet and the sextet complexes, with the quartet lying slightly higher, whereas B3LYP yields a substantial energy difference of 8.5 kcal/mol. The inclusion of the zero-point vibrational energies results in inverse ordering of sextet and quartet states with the pure density functionals. At the same time this does not change the sequence of states from the hybrid HF/DFT functional (B3LYP).

The results of density functional calculations on the charge-transfer complexes have to be viewed with care, because usually density functionals overestimate the interaction energy and the amount of charge transfer in such complexes.[23] Quantitatively the results from the hybrid density functional seem to be slightly more reliable than those from pure density functionals. The results of Fiedler et al.[7] are closer to the B3LYP data.

B. Primary Addition Product and the Bond Activation Barriers. *Products.* The primary addition products, **2**-^{6}A′ and **2**-^{4}A″ in Figure 1 (structures in Scheme 3), possess inverse order of relative stabilities of the sextet and quartet states as compared to the reactants. All three density functionals yield the same ordering of states. The Fe−O bond as well as the Fe−H bond is considerably shorter in the **2**-^{4}A″ adduct. This species may be viewed as resulting from coordination of the hydrogen atom to the ^{5}A″ state of $FeOH^+$, which is almost degenerate with the ground ^{5}A′ state (entries 9 and 10 in Table 2). Very schematically, the chemical bonding in this complex arises from interaction of the hydrogen s-orbital with two singly occupied orbitals of ^{5}A″ $FeOH^+$: σ-type nonbonding and $\pi(xz)$-type antibonding orbitals. The three-electron, two-center bond is formed with the doubly occupied bonding orbital pointed toward the hydrogen atom and the singly occupied antibonding orbital normal to the Fe−H bond.

The **2**-^{6}A′ adduct results from the interaction of the hydrogen atom with the excited ^{5}A′ state of $FeOH^+$, which is ca. 10 kcal/mol above the ground ^{5}A′ state (see a-^{5}A′ entry 11 in Table 2). In the excited state the nonbonding σ-type orbital is doubly occupied, whereas in the ground state of $FeOH^+$ it is the low-lying nonbonding δ-type (x^2-y^2)-orbital, which is doubly occupied. In the resulting **2**-^{6}A′ adduct an extra electron from hydrogen is transferred into the empty antibonding σ-type orbital of the $FeOH^+$ fragment, and the chemical bonding arises from the interaction of the empty hydrogen orbital with the doubly occupied nonbonding σ-type fragment orbital. Thus, the relative stabilities of the sextet and quartet insertion complexes correlate with relative stabilities of the constituting $FeOH^+$ fragments.

Barriers and Transition States. The formation of the addition adducts **2**-^{6}A′ and **2**-^{4}A″ occurs via the transition states **TS1**-^{6}A′ and **TS1**-^{4}A″. These transition structures have already been studied in the work of Fiedler et al.,[7] and as it has been ascertained, they are the only saddle points between the reactants complexes and the primary addition products. According to our calculations the activation energies on the sextet surface are large and consist of 12.0 (FT97), 6.9 (BP86), and 8.4 (B3LYP) kcal/mol. The experimental estimate for the barrier height varies from 13.8 to 17.3 kcal/mol,[10] while the datum of Fiedler et al.[7] is 19.0 kcal/mol. Be it as it may, the sextet barrier is well above the entrance channel.

The barrier on the quartet surface is very small and consists only of −0.9 (FT97), 0.0 (BP86), and 0.6 (B3LYP) kcal/mol. These barriers are all much smaller than the datum of Fiedler et al.[7] (6.0 kcal/mol) and appear to be more consistent with experimental observations.

C. Elimination Transition States, Barriers, and the $Fe(H_2O)^+$ Complex. The formation of the $Fe(H_2O)^+$ sextet and quartet complexes, **3**-^{6}A′ and **3**-^{4}A″ in Scheme 3 and Figure 1, occurs via 1,2-hydrogen migration in the primary addition adducts **2**-^{6}A′ and **2**-^{4}A″, respectively. On the sextet surface this migration passes via the planar transition state **TS2**-^{6}A′ (see Scheme 3) and is associated with the activation barrier varying from 25.1 (B3LYP) to 30.3 (FT97) kcal/mol.

On the quartet surface, the planar C_s structure for the activation complex **TS2**-^{4}A″, calculated with pure density functionals (FT97 and BP86), exhibits two imaginary frequencies. The eigenvectors associated with these frequencies correspond to the 1,2-hydrogen migration (the first eigenvector) and the rotation of the OH group around the Fe−O bond (the second one). Thus, the true transition state for the quartet surface arising from pure density functionals is nonplanar (C_1 point group) with a torsional angle between FeOH and H′FeO planes varying from 69.9° (FT97) to 60.9 (BP86)°. The activation energy associated with these structures is much lower than for the sextet state and consists of 13.3 (FT97) and 10.2 (BP86) kcal/mol. However the planar "bisaddle" structure is almost degenerate with the nonplanar transition state and is only 1.0 (FT97) and 0.7 (BP86) kcal/mol above the latter. An inclusion of the ZPEs reduces these differences to 0.6 (FT97) and 0.2 (BP86) kcal/mol. The B3LYP calculations predict the planar C_s structure to be the true saddle point with only one imaginary frequency. The nonplanar C_1 transition structure from the B3LYP possesses also one imaginary frequency and lies only 0.2 kcal/mol below the planar saddle point (0.02 kcal/mol with ZPE). The torsional angle in the nonplanar structure from the B3LYP is smaller than those from pure density functionals and is 52.5°.

Thus, the nonplanar transition structure from all density functionals is slightly more stable than the planar one, but the energy difference is very small and the imaginary frequency corresponding to the rotation around the Fe−O bond is very weak: i247.2 cm^{-1} (FT97) and i217.2 cm^{-1} (BP86). Taking into account a relatively large torsional angle in the nonplanar transition state (around 60°) and the planarity of the final and initial structures, one can assume that the real dynamic process would occur via a transition structure close to the planar rather than to the nonplanar one.

The products of the 1,2-hydrogen migration, the sextet **3**-^{6}A′ and the quartet **3**-^{4}A″ water complexes, are considerably more stable than the primary addition adducts **2**-^{6}A′ and **2**-^{4}A″. All density functionals used predict the quartet water complex to be the most stable in contrast to the ab initio methods, which predict the quartet state to be 1−4 kcal/mol above the sextet one.[24] This inverse ordering of states from DFT can be attributed to a bias toward $3d^n$ configurations over $3d^{n-1}4s^1$, which is inherent to pure density functionals as well as to the hybrid methods. This effect, which has been discussed extensively,[25,26] leads to an incorrect ordering of states for Fe^+ with the ^{4}F state from the $3d^7$ configuration being the ground state. Since the relative stability of the quartet and sextet states of $Fe(H_2O)^+$ is determined by ^{6}D−^{4}F separation for the Fe^+, the sextet state **3**-^{6}A′ derived from the ^{6}D state of the Fe^+ ($3d(x^2-y^2)$ doubly occupied) is less stable than the quartet **3**-^{4}A″ originating mostly from the ^{4}F asymptote.

Due to this incorrect description of one-center exchange in $3d^n$ and $3d^{n-1}4s^1$ configurations, density functional methods fail to predict the second sextet−quartet curve-crossing in the exit channel between the transition state of 1,2-hydrogen migration and the water complex. It may be anticipated that if one shifts up a part of the quartet potential surface near the elimination channel (water complex and products) by a constant value so that the experimental ^{6}D−^{4}F separation of 0.25 eV (5.8 kcal/mol) will be reproduced, then the quartet water complex will be ca. 1−3 kcal/mol above the sextet one, in general agreement with ab initio results.[24] These shifted values are given parenthetically in Figure 1. Of course, this surface shifting is not a rigorous procedure, but qualitatively it may be tolerated because the incorrectly described effect (difference in exchange energy in $3d^n$ and $3d^{n-1}4s^1$ configurations) is of one-center origins and does not affect bonding between the metal atom and water molecule. Hence, on the basis of these qualitative considerations one can expect the second spin junction near the water complex (see dashed line in Figure 1).

D. Products. The water complexes formed at the previous stage can dissociate easily to final products due to overall exothermicity of the reaction. The experimental measurements yield the FeO^+/H_2 reaction to be exothermic with $\Delta H_R^\circ = -37$ kcal/mol.[10] The B3LYP predicts a very close value of −38.5 kcal/mol for the reaction energy. Other density functionals used strongly underestimate the exothermicity of reaction. This is due to the aforementioned overestimated FeO^+ bond energy in the ground $^6\Sigma^+$ state. The BP86 and FT97 predict a bond energy of 108 kcal/mol, which is in excess of about 28 kcal/mol. The B3LYP functional yields a more reliable value for D_e in FeO^+ of 80.5 kcal/mol. In the sextet water complex $Fe(H_2O)^+$, the B3LYP and FT97 density functionals yield for the water dissociation energy 34.9 and 30.7 kcal/mol, respectively, in reasonable agreement with the ab initio result of 35.4 kcal/mol.[24] The BP86 strongly overestimates water binding in the sextet $Fe(H_2O)^+$, yielding the value of 50.1 kcal/mol.

3. Oxene-Insertion Mechanism. This mechanism requires a direct attack of the H_2 molecule on the O-end of FeO^+, forming the metal-bound water molecule. For this mechanism all density functional calculations have been done within C_s symmetry constraint with the H_2 molecule approaching the O-end of FeO^+ such that the H−H bond is perpendicular to the symmetry plane formed by the Fe and O atoms and the H−H bond midpoint. A reaction coordinate is the distance from the oxygen to the dihydrogen bond midpoint. The results are summarized in Table 2. Scheme 4 shows the crucial structures.

In the sextet state no initial complex between the reactants and no true transition state have been obtained from all three density functional calculations. Moving along the reaction coordinate results in an energy maximum which is characterized by two imaginary frequencies with comparable negative curvatures in both directions (see entry 2 in Table 2). The height

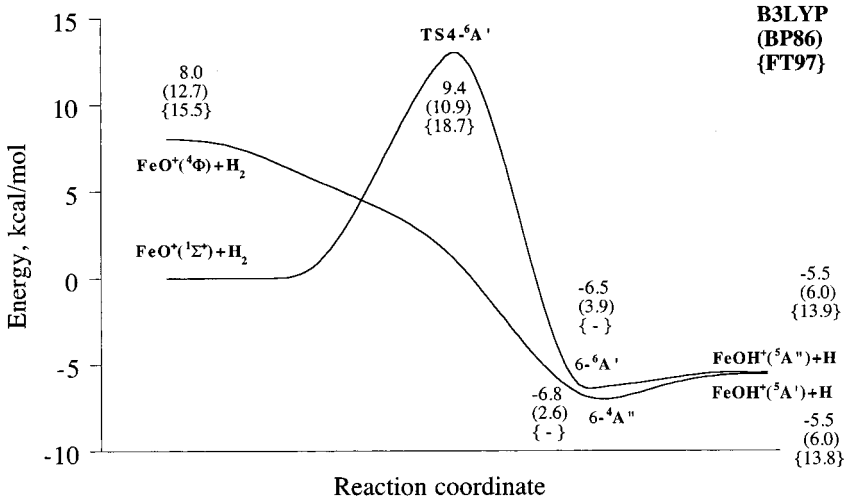

Figure 2. Energy profile for hydrogen abstraction in the "rebound" mechanism. The potential curves are plotted using B3LYP data (without parentheses). The BP86 results are given in parentheses; the FT97 data are presented in curly brackets.

SCHEME 4: BP86 Geometries (Table 2) for Species in the Oxene-Insertion Mechanism

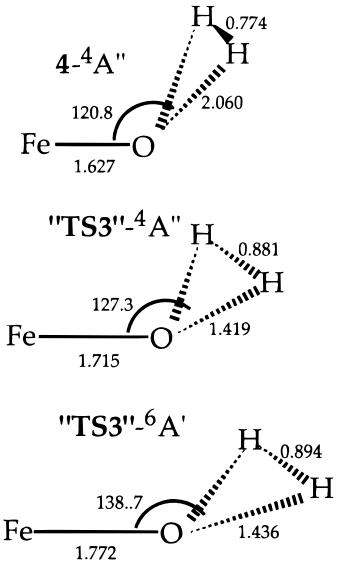

of the maximum with respect to the reactants ground-state level is 39.1 (FT97), 29.2 (BP86), and 30.8 (B3LYP) kcal/mol. The first eigenvector corresponding to the imaginary frequency represents the dihydrogen translation along the reaction coordinate. The second one corresponds to a rotation of the dihydrogen around the bond midpoint with both hydrogen atoms remaining in the (H−H−O) plane. Following the second eigenvector would lead to the structure that is characteristic of the stepwise rebound mechanism (see below).

In the quartet state, a weak initial complex **4**-^{4}A″ between the reactants is predicted from pure density functionals. A structure of this side-on complex resembles that of **1**-^{4}A″, but now the dihydrogen is adjacent to the oxygen atom. The complexation with energy varying from 1.3 (FT97) to 3.6 (BP86) kcal/mol is due to a weak electron donation (ca. 0.16*e*) from the dihydrogen to FeO^+. In line with these tiny complexation energies, the B3LYP method did not even yield a stable structure for the initial complex with dihydrogen bound to the oxygen atom. The B3LYP optimization of **4**-^{4}A″ led instead to the reactants complex for the addition−elimination mechanism (see Figure 1). Again, much as in the sextet state, the calculation for the quartet surface yields only a maximum along the reaction pathway, with negative curvatures in the directions of the dihydrogen transfer along the reaction coordinate and of the dihydrogen rotation around the bond midpoint. These maxima are situated at 13.9 (B3LYP), 14.4 (BP86), and 23.1 (FT97) kcal/mol above the entrance channel.

Thus, both transition structures, sextet and quartet, obtained for the synchronous dihydrogen insertion are not true saddle points but maxima, and an unconstrained search along the reaction coordinate will result in the structures characteristic to the "rebound" mechanism (see below). Since the critical species are not genuine transition structures, we refrain from drawing the potential energy surface.

SCHEME 5: Geometries (Table 2) for Species in the "Rebound" Mechanism

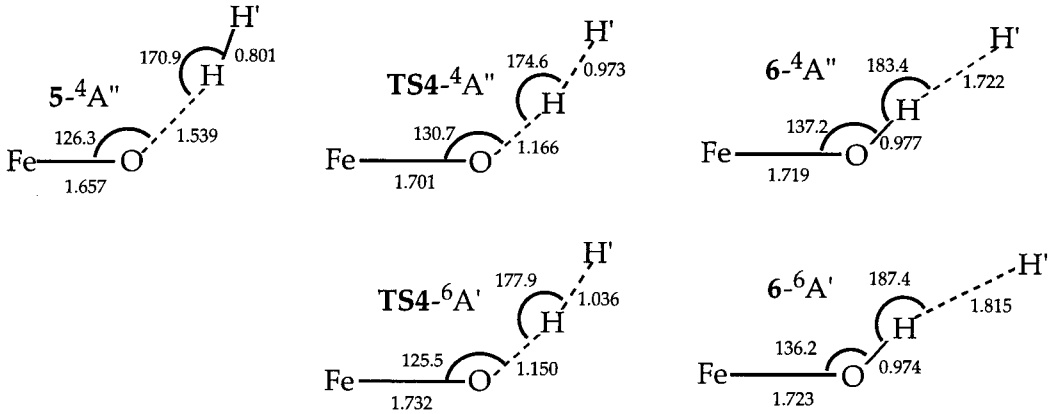

TABLE 3: Thermochemical and Kinetic Isotope Effect Data for the Addition−Elimination Mechanism[a]

entry		$FeO^+ + H_2$	**TS1**-^{4}A″ $HFeOH^+$	**TS1**-^{6}A′ $HFeOH^+$	$FeO^+ + D_2$	**TS1**-^{4}A″ $DFeOD^+$	**TS1**-^{6}A′ $DFeOD^+$
1	ZPE[b], kJ/mol						
	FT97	31.22	37.57	33.73	23.56	28.40	25.46
	BP86	31.22	37.46	34.28	23.61	28.37	25.85
	B3LYP	31.66	38.88	35.33	23.87	29.32	26.68
2	ΔH_v[c], kJ/mol						
	FT97	0.17	0.64	0.63	0.17	1.16	1.16
	BP86	0.16	0.46	0.63	0.16	0.96	1.15
	B3LYP	0.18	0.49	0.57	0.18	1.00	1.05
3.	q_v[d]						
	FT97	1.017 14	1.076 08	1.068 29	1.017 14	1.186 91	1.153 46
	BP86	1.015 27	1.044 02	1.069 18	1.015 27	1.124 52	1.154 46
	B3LYP	1.017 44	1.049 51	1.060 43	1.017 44	1.134 12	1.135 81
4	I, $I_xI_yI_z$[e]						
	FT97	0.046 47	25.043 76	34.252 08	0.092 87	55.296 22	75.324 52
	BP86	0.046 75	26.134 85	33.591 05	0.093 43	58.153 41	74.109 58
	B3LYP	0.045 85	25.914 30	33.418 65	0.09 164	57.564 82	73.826 69
5	$U^{\#f}$, kJ/mol						
	FT97		−3.62	50.35		−3.62	50.35
	BP86		-0.13	28.66		−0.13	28.66
	B3LYP		2.58	35.34		2.58	35.34
6	$E^{\#g}$, kJ/mol						
	FT97		3.20	53.32		2.21	53.24
	BP86		6.41	32.19		5.43	31.89
	B3LYP		10.11	39.40		8.85	39.02
7	k_{H_2}/k_{D_2}						
	FT97					2.22	3.28
	BP86					2.27	3.00
	B3LYP					2.03	2.92

[a] All data are given in kJ/mol. 1 kcal/mol = 4.184 kJ/mol. Calculations correspond to $T = 298$ K. $RT = 2.477$ kJ/mol. [b] Zero-point vibrational energy evaluated as a half sum of harmonic frequencies. [c] Thermal vibrational correction $\Delta H_v(T) = \sum_i \hbar\omega_i(\exp(\hbar\omega_i/kT) - 1)^{-1}$.[21] [d] Vibrational partition function $q_v = \prod_i (1 - \exp(-\hbar\omega_i/kT))^{-1}$.[21] [e] Principal moments of inertia: I_{H_2} and I_{D_2} in g·cm^2, and $I_x^{\#}\, I_y^{\#}\, I_z^{\#}$ in g^3·cm^6. [f] Activation energy without vibrational contribution. [g] Activation energy with zero-point energy and vibrational thermal correction. [h] Kinetic isotope effect evaluated using eq 4.

4. "Rebound" Mechanism. The "rebound" mechanism involves in principle two kinetic steps specified in Scheme 2a: an initial abstraction of the hydrogen atom from dihydrogen followed by a recombination of the free hydrogen with the metal-bound OH group. The critical species are depicted in Scheme 5, while Figure 2 shows the potential energy profiles.

In our calculations for the first mechanistic step we allowed a head-on approach of the dihydrogen molecule toward the O-end of FeO^+ such that all atoms (Fe, O, and both hydrogens) remain in the same plane. For the sextet state all density functionals used do not predict a formation of the initial complex between the reactants. The total energy increases with decreasing OH distance without passing via a minimum. The sextet transition state **TS4**-^{6}A′ is predicted at the OH distances of 1.150 Å (FT97), 1.210 Å (BP86), and 1.340 Å (B3LYP). In the transition state an electron donation from dihydrogen to the oxygen atom occurs varying from 0.21*e* (B3LYP) to 0.26*e* (BP86). The activation energy for this kinetic step amounts to 18.7 (FT97), 10.9 (BP86), and 9.4 (B3LYP) kcal/mol, in correlation with the corresponding H−H bond elongation values (see Table 2). Further contraction of the OH distance accompanied by the H−H bond elongation results in the formation of a weak intermediate complex **6**-^{6}A′ of the hydrogen atom with the $FeOH^+$. The interaction energy varies from 1.0 (B3LYP) to 2.1 (BP86) kcal/mol. Unfortunately we failed to optimize a geometry for this intermediate complex with the FT97 density functional because of a failure of SCF convergence.

A dissociation of the intermediate **6**-^{6}A′ cluster yields the products of the first step: $FeOH^+$ in the ground ^{5}A′ state and free hydrogen. Pure density functionals FT97 and BP86 predict

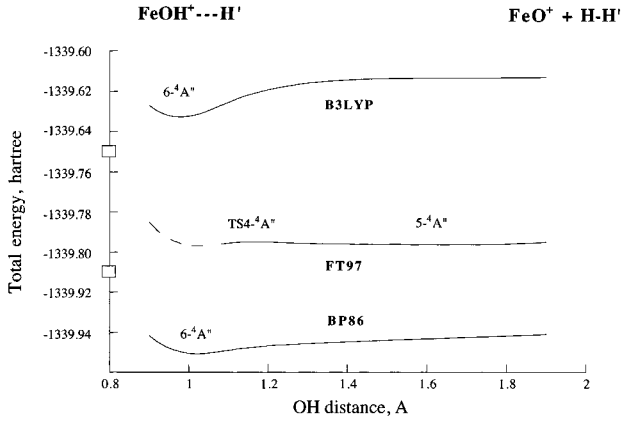

Figure 3. Potential energy curves for the low-spin hydrogen abstraction step of the "rebound" mechanism as functions of OH distance (see Scheme 5). The final $FeOH^+\cdots H$ (**6**-^{4}A″) complex has not been located with the FT97 functional due to a convergence problem (see text), and the potential curve in this region (shown with dashed line) has been simulated. The initial $FeO^+\cdots H_2$ (**5**-^{4}A″) complex and a transition state (**TS4**-^{4}A″) were predicted only by the FT97 functional (see text).

the hydrogen abstraction step to be endothermic with a relatively high endothermicity of 6.0 (BP86) and 13.8 (FT97) kcal/mol. The B3LYP calculation yields the exothermic reaction with an energy of −5.5 kcal/mol. This result is in reasonable agreement with the experimental estimates for the enthalpy of reaction $FeO^+ + H_2 \rightarrow FeOH^+ + H$, which amounts to ca. −5 kcal/mol.[2,3,10] Again the failure of pure density functionals can be traced back to the overestimated bond energy in FeO^+ and to the general overbinding problem. The hybrid B3LYP functional yields more balanced results.

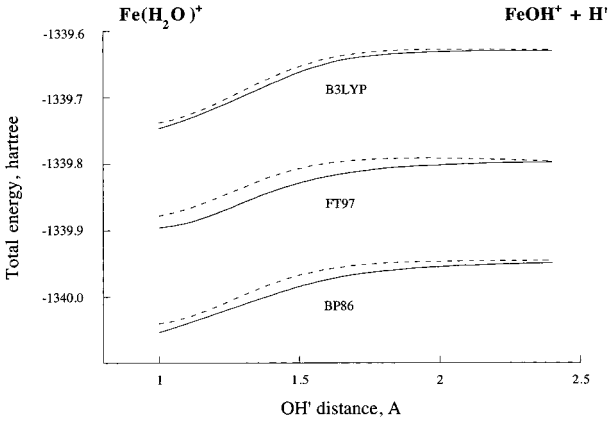

Figure 4. High-spin (dashed line) and low-spin (solid line) potential curves for the "rebound" step. The hydrogen atom H′ approaches a free coordination site on the oxygen atom in $FeOH^+$ and the excess electron is shifted onto the iron, forming the metal-bound water molecule (see text).

The quartet reaction profile is displayed in Figure 3 for the three functionals. The B3LYP and BP86 yield a smooth potential curve along the reaction coordinate (OH distance), which possesses only one minimum corresponding to the products complex **6**-^{4}A″. The FT97 functional yields a very shallow minimum corresponding to the reactants complex **5**-^{4}A″ and a saddle point, which are at 3.0 and 1.9 kcal/mol below the level of $FeO^+(^4\Phi) + H_2$, respectively. Thus, the hydrogen abstraction from the FT97 calculations is virtually activationless, albeit the potential curve along the reaction coordinate is not as smooth as from other density functional calculations. Unfortunately, poor SCF convergence with FT97 did not enable the optimization of the product complex **6**-^{4}A″.

A dissociation of the product complex **6**-^{4}A″ (Figure 3) yields the free hydrogen atom and $FeOH^+$ in the ^{5}A″ state, which differs from the ground ^{5}A′ state by occupancy of the Fe δ-type orbitals: in ^{5}A′ the $d_{x^2-y^2}$-orbital is doubly occupied, whereas in ^{5}A″ it is the d_{xy}-orbital. Both states are almost degenerate, and the calculated energy difference is 0.05 (FT97), 0.08 (BP86), and 0.05 (B3LYP) kcal/mol. In the products complex **6**-^{4}A″ the spins on the hydrogen and on the $FeOH^+$ are arranged antiferromagnetically, and the interaction energy with respect to the ^{5}A′ state of $FeOH^+$ is 1.3 (B3LYP) and 3.4 (BP86) kcal/mol, a little bit more than in the sextet products complex **6**-^{6}A′.

The reaction mechanisms for the hydrogen abstraction step can be summarized by turning back to Figure 2. Again as in the case of the addition−elimination mechanism, the sextet and quartet potential surfaces cross each other, but now the curve-crossing point is above the reactants ground-state level. From the B3LYP calculations the curve-crossing point is estimated to be ca. 4 kcal/mol above the reactants level.

A recombination of the products of the first step by "rebound" of $FeOH^+$ and H yields the water complexes **3**-^{6}A′ and **3**-^{4}A″ (see Scheme 3) and according to our calculations occurs without activation barrier. All density functionals yield the smooth potential energy curves along the OH′ approach coordinate as shown in Figure 4. Moreover, the dissociation of the $FeOH^+\cdots$H complexes will most likely compete with the "rebound" step in which the hydrogen atom recombines with the hydroxide moiety of the $FeOH^+$ species to form the iron−water complex. This latter process involves a very small potential barrier, the upper bound for which can be estimated from the dissociation energy of the $FeOH^+\cdots$H complex, i.e., less than 1−3 kcal/mol. Thus, the rebound TSR mechanism may be effectively represented as a one-step process with a rate-limiting hydrogen abstraction followed by a rapid almost instantaneous collapse of the intermediate complex. This virtually barrierless "rebound" step has a fundamental and simple origin. Thus, the interaction of the H-radical with the oxygen lone-pair results in a three-electron O···H interaction. *Since the iron has low-lying vacant (or singly occupied) orbitals, the third electron of the O···H linkage is shifted onto the iron and a two-electron O−H bond is established.* Since the iron d-orbitals are quite low-lying, this electron shift would occur at a long H···O distance where no barrier is expected. It is the spin inversion process from the quartet to the sextet surface that will endow the $FeOH^+/H^\bullet$ radical pair with some finite lifetime which will permit escape of free radicals.

Discussion

The three potential chemical mechanisms for H_2 oxidation (Schemes 1 and 2) have some common features as well as some differences. The most important common feature is that they are in fact all TSR electronic mechanisms with barriers and spin-inversion junctions.[3,7−9] Furthermore, in all the mechanisms the sextet surface is bumpy, while the quartet surface is relatively flat. Thus, be the chemical mechanism as it may, *the low-spin surface is seen to provide a low-energy path for the H_2 oxidation, in accord with previous concepts of TSR.*[3,7−9]

Aside from the common features, the chemical mechanisms are widely different. All the computational levels suggest that the oxene-insertion mechanism (Scheme 2b) is the least favorable. Thus, even if the maximum energy structures along the path ("TS3" in Scheme 4) were true saddle points, it would be clear that their energies are still too high to render the oxene-insertion competitive with the other mechanisms.

It is expected therefore that the addition−elimination and "rebound" mechanisms will dominate the reactivity patterns of the FeO^+/H_2 system. The mechanistic competition should be temperature dependent.

A. TSR in the Low-*T* Limit. At low temperatures (e.g., room temperature) the TSR pathway for the addition−elimination mechanism (Figure 1) is favored over TSR for the "rebound" mechanism (Figure 2), because in the latter the spin-inversion junction lies ca. 4 kcal/mol above the entrance channel.

The addition−elimination TSR (Figure 1) provides an almost barrierless pathway for the bond activation which will be limited mostly by the spin-inversion probability, which according to previous calculations is low, ca. 10^{-2}. The negative temperature coefficient measured[10] for the rate constant is consistent with the computational result of a zero energy barrier. This negative temperature coefficient appears to originate in the nonadiabaticity of the spin-inversion process,[8] which is more efficient at lower temperatures or/and lower kinetic energy excitations.

The validity of the TSR pathway may be further tested by calculations of the kinetic isotope effect (KIE) factors for $FeO^+/H_2(D_2)$ for a TSR pathway versus a single-state-reactivity (SSR) pathway via the sextet surface. Table 3 summarizes the requisite thermochemical data and resulting KIE factors calculated from eq 4 (see Methods section). These values (entry 7) are in the range 2.03−2.27 for the TSR option, and >3 for the SSR option. The experimental data[10,27] at ca. 300 K range between 1.45 and 2.09 depending on the experimental technique. The comparison appears to be more satisfactory for the TSR pathway. Thus, the measured kinetic isotope effects probe the extent of H···H (D···D) bond cleavage in a *mechanism whereby bond activation and spin-inversion occur in a concerted manner.*

We have also carried out a calculation of the temperature profile of the isotope effect (not tabulated) for the addition−

elimination TSR path. Our results show that at temperatures (kinetic energies) lower than room temperature (i.e., at $T = 150$ K) the isotope effect k_{H_2}/k_{D_2} is 0.90−1.14 (depending on the functional). As the temperature increases, the isotope effect increases too, and at $T = 450$ K it is 2.60−2.90. As the temperature increases further, the isotope effect converges to 1.35−1.36. This *T*-profile of the isotope effect which maximizes at sufficiently high temperatures ($T \geq 450$ K) may be useful for an experimental characterization of the mechanism.

B. SSR in the High-*T* Limit. At a high enough temperature or kinetic energy excitation (≥0.5 eV), the system has sufficient energy to pass the sextet barriers (7−19 kcal/mol) both for the addition−elimination and for the "rebound" mechanisms (Figures 1 and 2). At these elevated temperatures, the spin-inversion probability is very low due to the nonadiabaticity of the process, and we can conclude that the TSR path is shut down, and the competition is between the SSR pathways of the addition−elimination and the "rebound" mechanisms.

Using the experimental[10] threshold of 0.5 eV ($^3/_2RT = 0.5$ eV = 48.24 kJ/mol), we have calculated the relative rate constants for the competing processes using the transition state theory expression

$$\frac{k_{ad}}{k_{rb}} = \frac{(I_x^{ad} I_y^{ad} I_z^{ad})^{1/2}}{(I_x^{rb} I_y^{rb} I_z^{rb})^{1/2}} \frac{q_v^{ad}}{q_v^{rb}} \exp\left(-\frac{E_{ad}^{\#} - E_{rb}^{\#}}{RT}\right) \qquad (5)$$

Here the superscripts ad and rb correspond to the addition−elimination and the rebound mechanisms, respectively; $I_x(y,z)$ are the principal moments of inertia of the transition states **TS1**-^{6}A′ and **TS4**-^{6}A′; q_v are the vibrational partition functions, and $E^{\#}$ are the activation energies with respect to the reactants ground state and include the ZPEs and the thermal vibrational corrections. The results of our calculations are presented in Table 4. All density functionals predict $k_{rb} > k_{ad}$. Thus, at high kinetic energies (high *T*) the addition−elimination and "rebound" mechanisms are competitive, with a preference for the "rebound". This would correspond to the appearance of $FeOH^+ + H^\bullet$ at a threshold of ≈0.5 eV as observed by experiment.[10] Furthermore, this is consistent also with the observation that the mass-spectrometric techniques that are able to thermalize the reactants do not observe $FeOH^+ + H^\bullet$ at energies corresponding to room temperature.[10] The low-temperature (room and below) k_{H_2}/k_{D_2} value of the "rebound" mechanism was calculated to be >5. This high value could be diagnostic for distinguishing the room-temperature addition−elimination TSR path from a "rebound" SSR mechanism.

C. TSR in the Intermediate-*T* Region. At intermediate temperatures that correspond to the crossing point ($^3/_2RT \cong 4$ kcal/mol = 16.74 kJ/mol) between the sextet and quartet states of the "rebound" mechanism (Figure 2), the "rebound" TSR pathway will be competitive with the addition−elimination TSR. This competition is more complex because now both energetics (due to the height of the crossing point) and nonadiabatic effects will determine the outcome. The temperature behavior may therefore be unusual.

When this competition becomes effective, it is likely that some $FeOH^+$ will be seen. However, since the "rebound" step (Figure 4) is essentially barrierless, the amount of $FeOH^+$ may be very small and escape detection. A more likely situation is the production of $Fe(OH_2)^+$ (**3**-^{4}A″) in the quartet state. As has been discussed previously,[8] the spin-inversion probability in this region should be extremely small. The intermediate-temperature regime should thus be quite interesting.

TABLE 4: Thermochemical and Kinetic Data for the Addition−Elimination and "Rebound" Mechanisms[a]

entry		$FeO^+ + H_2$	TSl-6A′, $HFeOH^+$	TS4-6A′, $FeOHH^+$
1	ZPE, kJ/mol			
	FT97	31.22	33.73	25.91
	BP86	31.22	34.28	24.52
	B3LYP	31.66	35.33	29.97
2	ΔH_v, kJ/mol			
	FT97	40.17	129.71	136.46
	BP86	40.11	129.26	137.87
	B3LYP	39.96	128.37	133.72
3	q_v			
	FT97		283.915 15	839.833 93
	BP86		271.703 18	2255.033 20
	B3LYP		239.263 22	1072.926 06
4	$I_xI_yI_z$			
	FT97		34.252 08	36.276 83
	BP86		33.591 05	36.611 84
	B3LYP		33.418 65	49.644 27
5	$U^{\#}$, kJ/mol			
	FT97		50.35	78.26
	BP86		28.66	45.40
	B3LYP		35.34	39.32
6	$E^{\#}$, kJ/mol			
	FT97		142.40	169.24
	BP86		120.87	136.46
	B3LYP		127.42	131.45
7	k_{ad}/k_{rb}[b]			
	FT97			0.76
	BP86			0.19
	B3LYP			0.21

[a] See footnotes in Table 3. All data belong to average kinetic energy $^3/_2RT = 0.5$ eV. [b] Ratio of limiting kinetic step rate constants for addition and rebound mechanisms.

Conclusions

The DFT calculations in the paper provide a detailed understanding of the mechanism of H_2 oxidation by FeO^+. It is predicted that in the low-temperature regime ($T \approx 300$ K) the dominant chemical mechanism is addition−elimination (Scheme 1 and Figure 1) which produces $Fe^+ + H_2O$, *via a TSR pathway that requires a double spin-inversion.* Kinetic isotope effect calculations matching the experiment[10] provide further support for the mechanism.

At the high temperatures the "rebound" mechanism (Scheme 2a) becomes dominant and produces $FeOH^+ + H^\bullet$ via a SSR pathway on the sextet potential surface. The high-spin "rebound" mechanism is formally stepwise, but actually its "rebound" step appears to be rather activationless and instantaneous.

The intermediate-temperature region seems to be characterized almost exclusively by TSR pathways via the competition of the addition−elimination and "rebound" mechanisms. *The TSR pathway for the "rebound" is expected to compete with the addition−elimination in liquid phase reactions and when the ferryl unit is complexed by ligands that perturb the addition step in the addition−elimination mechanism.* The temperature dependence of rate in this region may be quite unusual and worthy of pursuit. If the TSR "rebound" mechanism operates in P-450 hydroxylation, one can understand the apparent contradiction between isotope effect profiles that match bona fide hydrogen abstraction processes[13b] and stereochemical radical lifetime results that suggest an effectively concerted mechanism.[14]

The oxene-insertion mechanism (Scheme 2b) does not appear to be a plausible option for the FeO^+/H_2 system.

Acknowledgment. The research was supported in part by a Grant from the G.I.F., the German-Israeli Foundation of Scientific Research and Development.

References and Notes

(1) Kappes, M. M.; Staley, R. H. *J. Phys. Chem.* **1981**, *85*, 942.

(2) Schröder, D.; Fiedler, A.; Ryan, M. F.; Schwarz, H. *J. Phys. Chem.* **1994**, *98*, 68.

(3) Clemmer, D. E.; Chen, Y.-M.; Khan, F. A.; Armentrout, P. *B. J. Phys. Chem.* **1994**, *98*, 6522.

(4) Baranov, V.; Javahery, G.; Hopkinson, A. C.; Bohme, D. K. *J. Am. Chem. Soc.* **1995**, *117*, 12801.

(5) Ortiz de Montellano, P. R., Ed. *Cytochrom P-450: Structure, Mechanisms, and Biochemistry*; Plenum Press: New York, 1986.

(6) For a recent review see: Schröder, D.; Schwarz, H. *Angew. Chem., Int. Ed. Engl.* **1995**, *34*, 1973.

(7) Fiedler, A.; Schröder, D.; Shaik, S.; Schwarz, H. *J. Am. Chem. Soc.* **1994**, *116*, 10734.

(8) Danovich, D.; Shaik, S. *J. Am. Chem. Soc.* **1997**, *119*, 1773.

(9) Shaik, S.; Danovich, D.; Fiedler, A.; Schröder, D.; Schwarz, H. *Helv. Chim. Acta* **1995**, *78*, 1393.

(10) Schröder, D.; Schwarz, H.; Clemmer, D. E.; Chen, Y.; Armentrout, P. B.; Baranov, V. I.; Bohme, D. K. *Int. J. Mass Spectrom. Ion Processes* **1997**, *161*, 175.

(11) For calculations on the FeO^+/CH_4 system, see: Yoshizawa, K.; Shiota, Y.; Yamabe, T. *Chem. Eur. J.* **1997**, *3*, 1160.

(12) Ryan, M. F.; Fiedler, A.; Schröder, D.; Schwarz, H. *J. Am. Chem. Soc.* **1995**, *117*, 2033.

(13) (a) Groves, J. T.: Chapter 1 in ref 5; (b) Manchester, J. I.; Dinnocenzo, J. P.; Higgins, L. A.; Jones, J. P. *J. Am. Chem. Soc.* **1997**, *119*, 5069. Dinnocenzo, J. P.; Karki, S. B.; Jones, J. P. *J. Am. Chem. Soc.* **1993**, *115*, 7111.

(14) Newcomb, M.; Le Tadic, M.-H.; Putt, D. A.; Hollenberg, P. F. *J. Am. Chem. Soc.* **1995**, *117*, 3312. Newcomb, M.; Le Tadic-Biadatti, M.-H.; Chestrey, D. L.; Roberts, E. S.; Hollenberg, P. F. *J. Am. Chem. Soc.* **1995**, *117*, 12085.

(15) Amos, R. D.; Alberts, I. L.; Andrews, J. S.; Collwell, S. M.; Handy, N. C.; Jayatilaka, D.; Knowles, P. J.; Kobayashi, R.; Laming, G. J.; Lee, A. M.; Maslen, P. E.; Murray, C. W.; Palmieri, P.; Rice, J. E.; Simandrias, E. D.; Stone, A. J.; Su, M.-D.; Tozer, D. J. *CADPAC6: The Cambridge Analytic Derivatives Package*; Cambridge, U.K., 1995.

(16) Amos, R. D.; Alberts, I. L.; Andrews, J. S.; Collwell, S. M.; Handy, N. C.; Jayatilaka, D.; Knowles, P. J.; Kobayashi, R.; Koga, N.; Laidig, K. E.; Maslen, P. E.; Murray, C. W.; Rice, J. E.; Sanz, J.; Simandrias, E. D.; Stone, A. J.; Su, M.-D. *CADPAC5: The Cambridge Analytic Derivatives Package*; Cambridge, U.K., 1992.

(17) Stevens, P. J.; Devlin, F. J.; Chablowski, C. F.; Frisch, M. J. *J. Phys. Chem.* **1994**, *98*, 11623.

(18) Filatov, M.; Thiel, W. *Mol. Phys.* **1997**, *91*, 847.

(19) Wachters, A. J. H. *J. Chem. Phys.* **1970**, *52*, 1033.

(20) Dunning, T. H. *J. Chem. Phys.* **1971**, *55*, 716.

(21) Frost, A. A.; Pearson, R. G. *Kinetics and Mechanism*; Wiley: New York, 1961.

(22) Loh, S. K.; Fisher, E. R.; Lian, L.; Schultz, R. H.; Armentrout, P. *B. J. Phys. Chem.* **1989**, *93*, 3159.

(23) Ruiz, E.; Salahub, D. R.; Vela, A. *J. Phys. Chem.* **1996**, *100*, 12265.

(24) Rosi, M.; Bauschlicher, C. W., Jr. *J. Chem. Phys.* **1989**, *90*, 7264.

(25) Gunnarsson, O.; Jones, R. O. *Phys. Rev. B* **1985**, *31*, 7588.

(26) Holthausen, M. C.; Heinemann, C.; Cornehl, H. H.; Koch, W.; Schwarz, H. *J. Chem. Phys.* **1995**, *102*, 4931.

(27) We use k_{H_2}/k_{D_2} from Table 2 in ref 10. The KIE values in this table are obtained with correction due to different collision frequencies of D_2 and H_2.